Diagnosing Stagnant Gas Bubbles in a Polymer Electrolyte Membrane Water Electrolyser using Acoustic Emission

M. Maier[1], Q. Meyer[2], J. Majasan[1], R.E. Owen[1,3], J.B. Robinson[1,3], J. Dodwell[1], Y. Wu[1], L. Castanheira[4], G. Hinds[4], P.R. Shearing[1,3], D.J.L. Brett[1,3,*]

[1] Electrochemical Innovation Lab, Department of Chemical Engineering, UCL, London, WC1E 7JE, UK
[2] School of Chemistry, UNSW, Sydney, 2052, New South Wales, Australia
[3] The Faraday Institution, Quad One, Harwell Science and Innovation Campus, Didcot, OX11 0RA, UK
[4] National Physical Laboratory, Hampton Road, Teddington, Middlesex, TW11 0LW, UK

*** Correspondence:**
D.J.L. Brett
d.brett@ucl.ac.uk

Keywords: Acoustic Emission, PEM Water Electrolyser, Operando Diagnostics, Mass Transport, Flow Channels

Abstract

The use of acoustic emission as a low-cost, non-destructive, and *operando* diagnostic tool has been demonstrated for a range of electrochemical energy conversion and storage devices, including polymer electrolyte water electrolysers (PEMWEs) and fuel cells. In this work, an abrupt change in acoustic regime is observed during operation of a PEMWE as the current density is increased from 0.5 A cm^{-2} to 1.0 A cm^{-2}. This regime change is marked by a sudden drop in the number of acoustic hits, while hit duration, amplitude, and energy increase significantly. It is found that the change in acoustic regime coincides with a significant extension of the stagnant bubble region in the flow channels of the PEMWE, observed with high-speed optical imaging. These results demonstrate that acoustic emission can be used effectively as an operando diagnostic tool to monitor bubble formation (two-phase flow conditions) in PEMWEs, facilitating rapid testing or prototyping, and contributing to operational safety.

1 Introduction

PEMWEs represent one of the most promising approaches to the production of 'green' hydrogen and large-scale energy grid stabilization. The technology is likely to replace the widely commercially used alkaline electrolysis due to advantages including lower voltage at equal current density, lower gas crossover, compact build, and the possibility of high-pressure operation [1]. While currently more expensive than the alternative alkaline technology, the capital cost of a typical PEMWE system is dropping [2] and plants rated up to 6 MW are in operation [3].

Water flooding has been shown to be a major mass transport limitation occurring in polymer electrolyte membrane fuel cells (PEMFCs) at high current densities, particularly at high humidity when water condenses at the cathode forming droplets which coalesce. This leads to water blocking the flow channels and occupying the gas diffusion layer, causing a consequent increase in pressure drop and decrease in performance [4–6]. Similarly to water accumulation in a PEMFC, which eventually leads to flooding, product gas can accumulate in polymer electrolyte membrane water electrolysers (PEMWEs) leading to bubbles blocking the flow channels. This occurs if the gas production from the catalyst sites exceeds the gas removal capacity of the flow channels, which is mainly determined by the cross-sectional area and the flow rate of water through the channels. The effects of bubble blockage on performance, pressure drop, and life-time of a PEMWE have not yet been investigated, but it is expected that prolonged bubble blockage results in local water starvation, causing a non-uniform current distribution over the active area and a decrease in performance [7].

Acoustic emission (AE) is a non-destructive, *operando* diagnostic tool traditionally used in civil engineering, e.g. for monitoring crack propagation in steel [8] or the stability of bridges [9]. It uses a piezoelectric sensor to detect mechanical perturbations emitted by an object and has been applied to a range of electrochemical energy storage devices. It has been used to monitor particle fracture and morphological changes in battery electrodes during charge and discharge [10–12], has been found to be sensitive to Li-ion intercalation and formation of the solid electrolyte interphase [13,14] in Li ion batteries, and has also been applied to PEMFCs [15–17].

Two-phase systems, such as the water-gas mixture in the flow channels of the PEMWE analysed in this work, are also readily analysed using acoustic emission. This includes the calculation of bubble size distribution [18], recognition of different flow patterns by analysing acoustic emission data with neural networks [19], and observing the formation and collapse of single bubbles [20]. Hence, acoustic emission is a valuable alternative diagnostic tool to other techniques for the investigation of two-phase dynamics [21–23].

In previous work, the authors demonstrated the ability of acoustic emission to detect changes in the number and size of bubbles passing through the flow channel of a PEMWE. This enabled the prediction of the change from bubbly to slug flow and showed that acoustic emission is a valuable *operando* tool for PEMWE diagnosis [24]. Here, we demonstrate that the acoustic emission signal changes dramatically when, rather than normal two-phase flow, stagnant bubbles are located within the vicinity of the acoustic emission sensor. This feature can be used to detect and locate bubble 'blockage' (channel dehydration) in PEMWEs, for *operando* monitoring or design optimization.

2 Experimental

2.1 PEMWE Cell

The electrolyser used in this work (Figure 1) had a 9 cm^2 active area and consisted of transparent Perspex end-plates, parallel titanium flow-fields, a titanium sinter liquid-gas diffusion layer (LGDL) on the anode side, a Toray H-060 carbon paper as the gas diffusion layer (GDL) on the cathode side, and a catalyst coated membrane (CCM), which was based on

Nafion 115 with 0.6 mg cm^{-2} platinum on the cathode and 3.0 mg cm^{-2} iridium/ruthenium oxide on the anode (ITM Power, UK). The flow-field consisted of nine parallel channels, with a length of 3 cm and a land and channel width of 1.76 mm. The electrolyser was run at ambient pressure with a deionised water inflow temperature of 50 $^{\circ}C$ and a water inflow rate of 10 ml min^{-1} at the anode and cathode. Electrochemical testing was performed between 0.0 and 2.0 A cm^{-2} using a potentiostat (Gamry Reference 3000 Galvanostat/Potentiostat with a Gamry 30k Booster; Gamry Instruments, USA).

2.2 Acoustic Emission

Acoustic emission was measured with a cylindrical piezoelectric sensor (S9208, Mistras NDT, UK), with a diameter and height of 25 mm. The sensor was placed in the centre of the flow-field on the anode side; data acquisition lasted 1 min during galvanostatic operation of the PEMWE. Due to the nature of sound transmission, no clear area can be defined within which acoustic data is collected. Whether a mechanical perturbation is detected by the sensor is contingent on the location and intensity of the perturbation, with the intensity necessary for detection increasing with the distance between acoustic source and sensor. Therefore, detection of stagnant bubbles is increasingly likely as they are located closer to the sensor (bubbles 'grow' from the top end of the channel towards the centre). Data were processed using the software AEWin (Physical Acoustics, USA). The sensor produces a continuous voltage/time signal, with strong mechanical perturbations producing high voltage values. After filtering and pre-amplification by 26 dB, acoustic hits exceeding a noise threshold of 37 dB were extracted from the continuous signal. An acoustic hit is defined as an acoustic event initiated by the acoustic emission signal exceeding the noise threshold and ending when the signal falls back below that threshold (Figure 2). Strong acoustic activity is marked by a high number of separate acoustic hits (events). The number of hits per unit time (hit rate H), the maximum of each waveform averaged over all hits (average hit amplitude A), the averaged time from exceeding the threshold until falling back below it (average hit duration D) and the average hit energy E were recorded. The hit energy was determined by integrating the area under the waveform with respect to time. Further details on acoustic emission data analysis can be found in previous work [24].

2.3 High-Speed Imaging

To visualize the movement of bubbles and the effect of increasing current density on the rate of removal of bubbles in the flow channels, high-speed imaging was employed. A Photron FASTCAM SA1 high-speed camera with a Tokina MACRO 100 F2.8 D lens was used to image the full flow-field on the anode side (1024×1024 pixel resolution, 2000 frames per second, 5.46 s acquisition). The transparent end-plates allowed for direct optical access to the flow-field [25,26].

3 Results and Discussion

The bubble evolution as a function of the current density has been captured with high-speed imaging experiments, which are shown as a function of increasing current density (Figure 3). As the cross-sectional area of the flow channels is finite and as all bubbles have to leave the flow-field through the manifold at the top end of the flow channels, the ability of the PEMWE cell to remove product gas is limited. This leads to bubbles blocking the top end of the flow channels at high current densities. For a given flow rate, the length of channel that contains stagnant bubbles at the top end of the flow channel increases significantly with current density. Here, a stagnant bubble is defined as a bubble which does not change its location, and particularly a bubble at the top end of the channel not entering the combining manifold, but remaining at the top end of the flow channel. The location of the largest stagnant bubble in each image in Figure 3 is marked in red. The amount of oxygen produced at the anode increases as a function of current density (Faraday's law); hence, a growth in the length of stagnant bubbles is expected with increasing current density. At a current density of 0.3 A cm^{-2} (Figure

3 (a)) the top end of each channel is almost free of stagnant bubbles, while a clear growth of these bubbles can be observed at 0.6 A cm^{-2} (Figure 3 (b)). At 1.0 A cm^{-2} (Figure 3 (c)), bubble blockage covers more than a quarter of the channel length.

The acoustic emission parameters are strongly influenced by the current density (Figure 4). As illustrated above, current density leads to bubble blockage at the top end of the flow channels; hence, Figure 4 can be interpreted as the correlation between the acoustic emission signal and the formation of stagnant bubbles. The acoustic hit rate drops from 80.0 s^{-1} to the limit of detection for the acoustic emission system used in this work (1.0 s^{-1}) between 0.5 A cm^{-2} and 1.0 A cm^{-2} (Figure 4 (a)). The limit of detection is an artefact of the data acquisition, which cuts off any hit longer than 1.0 s, which means that from 1.0 A cm^{-2} onwards the AE signal continuously exceeds the noise threshold, with no individual acoustic hits discernible. This significant decrease of acoustic hits highlights a dramatic change of two-phase flow within the flow channels. The relationship between the number of acoustic hits and the number of bubbles passing through the flow channels has been established in previous work [24], which found that the number of acoustic hits scales directly with the number of bubbles passing through the flow channels. Hence, a drop in the number of acoustic hits indicates a decrease in the number of bubbles generated and passing through the flow channels, which is likely due to the blocking of the flow channel by a stagnant bubble. This stagnant bubble stops smaller bubbles from traveling upwards through the flow channels; instead the bubbles coalesce into the stagnant bubble. Hence, the drop in the number of acoustic hits between 0.5 A cm^{-2} and 1.0 A cm^{-2} is likely caused by the extension of stagnant bubbles into the sensor area.

Further, the average hit amplitude (Figure 4 (b)) increases steeply by around 50 % between 0.5 A cm^{-2} and 1.0 A cm^{-2}, the same range within which the hit rate drops. The average hit duration increases from less than 0.1 ms to the cut off value of 1.0 s mentioned above (Figure 4 (c)). For current densities above 1.0 A cm^{-2}, a constant signal is detected, indicating permanent contact between a bubble and the end-plate. Finally, an increase in hit duration and amplitude causes an increase in acoustic energy (Figure 4 (d)). All these changes occur in a step-like manner between 0.5 A cm^{-2} and 1.0 A cm^{-2}.

The decreasing number of hits, while hit amplitude and contact time between bubble and end-plate increase, all suggest that the signal change is caused by the extension of the stagnant bubble region towards the sensor location in the current density range between 0.5 A cm^{-2} and 1.0 A cm^{-2} (Figure 4). This is supported by the extension of the stagnant bubble region (Figure 3) observed via high-speed imaging, a major part of which occurs between 0.6 A cm^{-2} and 1.0 A cm^{-2}.

4 Conclusion

Acoustic emission has been demonstrated as a useful technique for *operando* diagnosis of bubble blockage in PEMWEs. High-speed imaging of an optically-transparent PEMWE cell was used to visualize the bubble movement in the flow channels. The length of the part of the flow channel containing stagnant bubbles was found to increase with current density, eventually reaching the location of the acoustic emission sensor. With increasing flow channel blockage, a dramatic change in acoustic activity was observed. The acoustic hit rate dropped from 80.0 s^{-1} to 1.0 s^{-1}, average hit amplitude increased from 32 dB to 50 dB, average hit duration from 0.1 ms to 1.0 s, and average hit energy from 0.004 aJ to 3400 aJ. These changes occurred abruptly between 0.5 A cm^{-2} and 1.0 A cm^{-2}, which coincides with a significant extension of the stagnant bubble region in the flow channels. This leads us to conclude that the change in acoustic activity is caused by the flow regime in the channels changing from two-phase flow to stagnant bubbles. The accumulation of gas in the flow channels occurs when gas production exceeds the capacity of the system for gas removal, which can affect the water distribution in the PEMWE. Insufficient water supply at the anode causes a voltage increase [7], hence lowers PEMWE efficiency and reduces hydrogen production at equal voltage. It is expected that acoustic emission can be used to detect local bubble blockage and insufficient water supply in specific areas of a PEMWE.

The use of this *operando* diagnostic tool has successfully been applied to a PEMWE, but could be extended to other applications. The accumulation of gas within a system or plant can cause inefficiencies or pose a hazard in many areas of chemical production and transport. Moreover, it has been shown that the change of two-phase flow regime influences the pressure drop [27,28]. Hence, the technique presented in this work could be deployed to screen various flow-field configurations or monitor safe limits of operation, replacing less cost-effective or accessible diagnostic tools such as neutron or X-ray imaging [29–31].

Captions

Fig. 1: Assembly of a PEMWE with the AE sensor, two end-plates, two flow-fields, the liquid-gas diffusion layer (LGDL), the catalyst coated membrane (CCM), and the gas diffusion layer (GDL) on the anode side.

Fig. 2: Typical structure of an acoustic hit as voltage profile as a function of time. The acoustic hit is initiated when the signal exceeds the noise threshold and ends when the signal falls back below the threshold. The hit amplitude is the intensity of the most prominent peak within the hit, and its energy is the integrated area of the hit (adapted from [32]).

Fig. 3: Exemplary results from high-speed imaging of the anode flow field of the PEMWE at (a) 0.3 A cm^{-2}, (b) 0.6 A cm^{-2}, and (c) 1.0 A cm^{-2} at a water inflow rate of 10 ml min^{-1}. The largest stagnant bubble at the top end of the flow channels is marked in red for each current density.

Fig. 4: Acoustic emission parameters as a function of current density for a water inflow rate of 10 ml min^{-1}. Acoustic hit rate (a), average hit amplitude (b), average hit duration (c), and average hit energy (d) are shown.

Acknowledgements

The authors acknowledge financial support into the EIL's hydrogen and fuel cell activity from the EPSRC through grants (EP/R023581/1; EP/P009050/1; EP/N032888/1; EP/M014371/1; EP/M009394; EP/L015749/1; EP/K038656/1). Support from the National Measurement System of the UK's Department of Business, Energy & Industrial Strategy is also gratefully acknowledged. PRS acknowledges funding from The Royal Academy of Engineering (CiET1718/59).

References

[1] M. Carmo, D.L. Fritz, J. Mergel, D. Stolten, A comprehensive review on PEM water electrolysis, Int. J. Hydrogen Energy. 38 (2013) 4901–4934. doi:10.1016/j.ijhydene.2013.01.151.

[2] S.M. Saba, M. Müller, M. Robinius, D. Stolten, The investment costs of electrolysis – A comparison of cost studies from the past 30 years, Int. J. Hydrogen Energy. 43 (2018) 1209–1223. doi:10.1016/j.ijhydene.2017.11.115.

[3] A. Buttler, H. Spliethoff, Current status of water electrolysis for energy storage, grid balancing and sector coupling via power-to-gas and power-to-liquids: A review, Renew. Sustain. Energy Rev. 82 (2018) 2440–2454. doi:10.1016/j.rser.2017.09.003.

[4] I.S. Hussaini, C.Y. Wang, Visualization and quantification of cathode channel flooding in PEM fuel cells, J. Power Sources. 187 (2009) 444–451. doi:10.1016/j.jpowsour.2008.11.030.

[5] K. Tüber, D. Pócza, C. Hebling, Visualization of water buildup in the cathode of a transparent PEM fuel cell, J. Power Sources. 124 (2003) 403–414. doi:10.1016/S0378-7753(03)00797-3.

[6] D. Spernjak, A.K. Prasad, S.G. Advani, Experimental investigation of liquid water formation and transport in a transparent single-serpentine PEM fuel cell, J. Power Sources. 170 (2007) 334–344. doi:10.1016/j.jpowsour.2007.04.020.

[7] S. Sun, Y. Xiao, D. Liang, Z. Shao, H. Yu, M. Hou, B. Yi, Behaviors of a proton exchange membrane electrolyzer under water starvation, RSC Adv. 5 (2015) 14506–14513. doi:10.1039/C4RA14104K.

[8] T.M. Roberts, M. Talebzadeh, Acoustic emission monitoring of fatigue crack propagation, J. Constr. Steel Res. 59 (2003) 695–712. doi:10.1016/S0143-974X(02)00064-0.

[9] A. Nair, C.S. Cai, Acoustic emission monitoring of bridges: Review and case studies, Eng. Struct. 32 (2010) 1704–1714. doi:10.1016/j.engstruct.2010.02.020.

[10] T. Ohzuku, H. Tomura, K. Sawai, Monitoring of Particle Fracture by Acoustic Emission during Charge and Discharge of Li/MnO2 Cells, J. Electrochem. Soc. 144 (1997) 3496–3500. doi:10.1149/1.1838039.

[11] K. Rhodes, N. Dudney, E. Lara-Curzio, C. Daniel, Understanding the Degradation of

Silicon Electrodes for Lithium-Ion Batteries Using Acoustic Emission, J. Electrochem. Soc. 157 (2010) A1354–A1360. doi:10.1149/1.3489374.

[12] C. Villevieille, M. Boinet, L. Monconduit, Direct evidence of morphological changes in conversion type electrodes in Li-ion battery by acoustic emission, Electrochem. Commun. 12 (2010) 1336–1339. doi:10.1016/j.elecom.2010.07.014.

[13] N. Kircheva, P.-X. Thivel, S. Genies, D. Brun-Buisson, Y. Bultel, Study of SEI formation in Li-ion batteries by acoustic emission technique., ECS Trans. 35 (2011) 19–26. doi:10.1149/1.3644900.

[14] N. Kircheva, S. Genies, D. Brun-Buisson, P.X. Thivel, Study of Solid Electrolyte Interface Formation and Lithium Intercalation in Li-Ion Batteries by Acoustic Emission, J. Electrochem. Soc. 159 (2012) A18–A25. doi:Doi 10.1149/2.045201jes.

[15] B. Legros, P.-X. Thivel, Y. Bultel, M. Boinet, R.P. Nogueira, Electrochemical Impedance and Acoustic Emission Survey of Water Desorption in Nafion Membranes, Electrochem. Solid-State Lett. 12 (2009) B116–B118. doi:10.1149/1.3131728.

[16] B. Legros, P.X. Thivel, Y. Bultel, M. Boinet, R.P. Nogueira, Acoustic emission: Towards a real-time diagnosis technique for Proton exchange membrane fuel cell operation, J. Power Sources. 195 (2010) 8124–8133. doi:10.1016/j.jpowsour.2010.07.045.

[17] V.S. Bethapudi, M. Maier, G. Hinds, P.R. Shearing, D.J.L. Brett, M.O. Coppens, Acoustic emission as a function of polarisation: Diagnosis of polymer electrolyte fuel cell hydration state, Electrochem. Commun. 109 (2019) 106582. doi:10.1016/j.elecom.2019.106582.

[18] A.B. Pandit, J. Varley, R.B. Thorpe, J.F. Davidson, Measurement of bubble size distribution: an acoustic technique, Chem. Eng. Sci. 47 (1992) 1079–1089. doi:10.1016/0009-2509(92)80233-3.

[19] G.G. Yen, H. Lu, Acoustic emission data assisted process monitoring, ISA Trans. 41 (2002) 273–282. doi:10.1016/S0019-0578(07)60087-1.

[20] S. Husin, A. Addali, D. Mba, Feasibility study on the use of the Acoustic Emission technology for monitoring flow patterns in two phase flow, Flow Meas. Instrum. 33 (2013) 251–256. doi:10.1016/j.flowmeasinst.2013.07.011.

[21] P. Huguet, A. Morin, G. Gebel, S. Deabate, A.K. Sutor, Z. Peng, In situ analysis of water management in operating fuel cells by confocal Raman spectroscopy, Electrochem. Commun. 13 (2011) 418–422. doi:10.1016/j.elecom.2011.02.008.

[22] T. Maiyalagan, V.S. Saji, Electrocatalysts for Low Temperature Fuel Cells: Fundamentals and Recent Trends, John Wiley & Sons, 2017.

[23] K. Dastafkan, Q. Meyer, X. Chen, C. Zhao, Efficient Oxygen Evolution and Gas Bubble Release Achieved by a Low Gas Bubble Adhesive Iron–Nickel Vanadate Electrocatalyst, Small. 16 (2020) 1–12. doi:10.1002/smll.202002412.

[24] M. Maier, Q. Meyer, J. Majasan, C. Tan, I. Dedigama, J. Robinson, J. Dodwell, Y. Wu, L. Castanheira, G. Hinds, P.R. Shearing, D.J.L. Brett, Operando flow regime diagnosis using acoustic emission in a polymer electrolyte membrane water electrolyser, J. Power Sources. 424 (2019) 138–149. doi:10.1016/j.jpowsour.2019.03.061.

[25] I. Dedigama, P. Angeli, K. Ayers, J.B. Robinson, P.R. Shearing, D. Tsaoulidis, D.J.L.

Brett, In situ diagnostic techniques for characterisation of polymer electrolyte membrane water electrolysers - Flow visualisation and electrochemical impedance spectroscopy, Int. J. Hydrogen Energy. 39 (2014) 4468–4482. doi:10.1016/j.ijhydene.2014.01.026.

[26] J.O. Majasan, J.I.S. Cho, I. Dedigama, D. Tsaoulidis, P. Shearing, D.J.L. Brett, Two-phase flow behaviour and performance of polymer electrolyte membrane electrolysers: Electrochemical and optical characterisation, Int. J. Hydrogen Energy. 43 (2018) 15659–15672. doi:10.1016/j.ijhydene.2018.07.003.

[27] C.W. Choi, D.I. Yu, M.H. Kim, Adiabatic two-phase flow in rectangular microchannels with different aspect ratios: Part i - Flow pattern, pressure drop and void fraction, Int. J. Heat Mass Transf. 54 (2011) 616–624. doi:10.1016/j.ijheatmasstransfer.2010.07.067.

[28] T. Cubaud, C.M. Ho, Transport of bubbles in square microchannels, Phys. Fluids. 16 (2004) 4575–4585. doi:10.1063/1.1813871.

[29] M. Maier, J. Dodwell, R. Ziesche, C. Tan, T. Heenan, J. Majasan, N. Kardjilov, H. Markötter, I. Manke, L. Castanheira, G. Hinds, P.R. Shearing, D.J.L. Brett, Mass transport in polymer electrolyte membrane water electrolyser liquid-gas diffusion layers: A combined neutron imaging and X-ray computed tomography study, J. Power Sources. 455 (2020). doi:10.1016/j.jpowsour.2020.227968.

[30] J.O. Majasan, F. Iacoviello, J.I.S. Cho, M. Maier, X. Lu, T.P. Neville, I. Dedigama, P.R. Shearing, D.J.L. Brett, Correlative study of microstructure and performance for porous transport layers in polymer electrolyte membrane water electrolysers by X-ray computed tomography and electrochemical characterization, Int. J. Hydrogen Energy. (2019). doi:10.1016/j.ijhydene.2019.05.222.

[31] O. Panchenko, E. Borgardt, W. Zwaygardt, F.J. Hackemüller, M. Bram, N. Kardjilov, T. Arlt, I. Manke, M. Müller, D. Stolten, W. Lehnert, In-situ two-phase flow investigation of different porous transport layer for a polymer electrolyte membrane (PEM) electrolyzer with neutron spectroscopy, J. Power Sources. 390 (2018) 108–115. doi:10.1016/j.jpowsour.2018.04.044.

[32] W. Caesarendra, B. Kosasih, A.K. Tieu, H. Zhu, C.A.S. Moodie, Q. Zhu, Acoustic emission-based condition monitoring methods: Review and application for low speed slew bearing, Mech. Syst. Signal Process. 72–73 (2016) 134–159. doi:10.1016/j.ymssp.2015.10.020.

Figure 1.JPEG

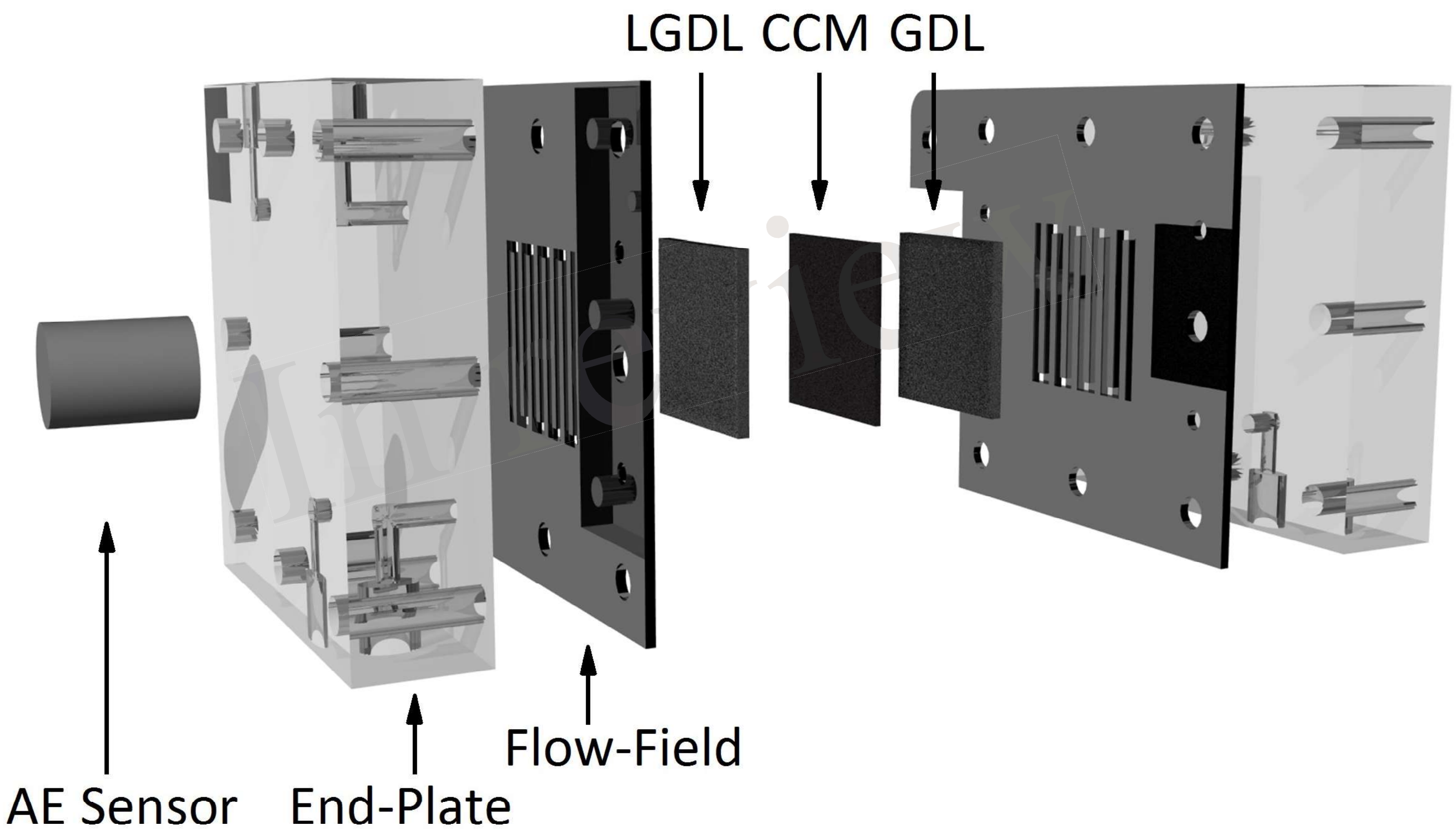

Figure 2.JPEG

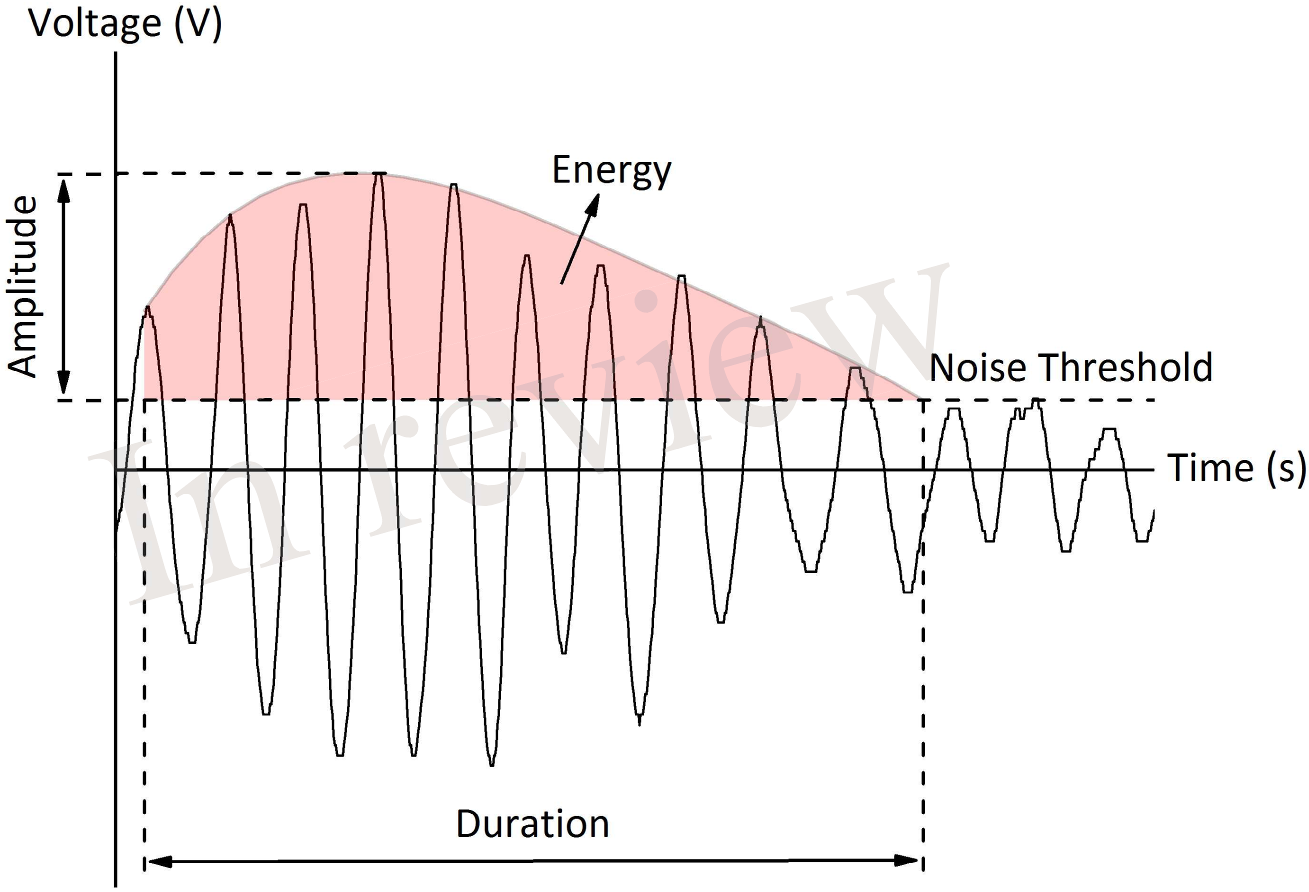

Figure 3.JPEG

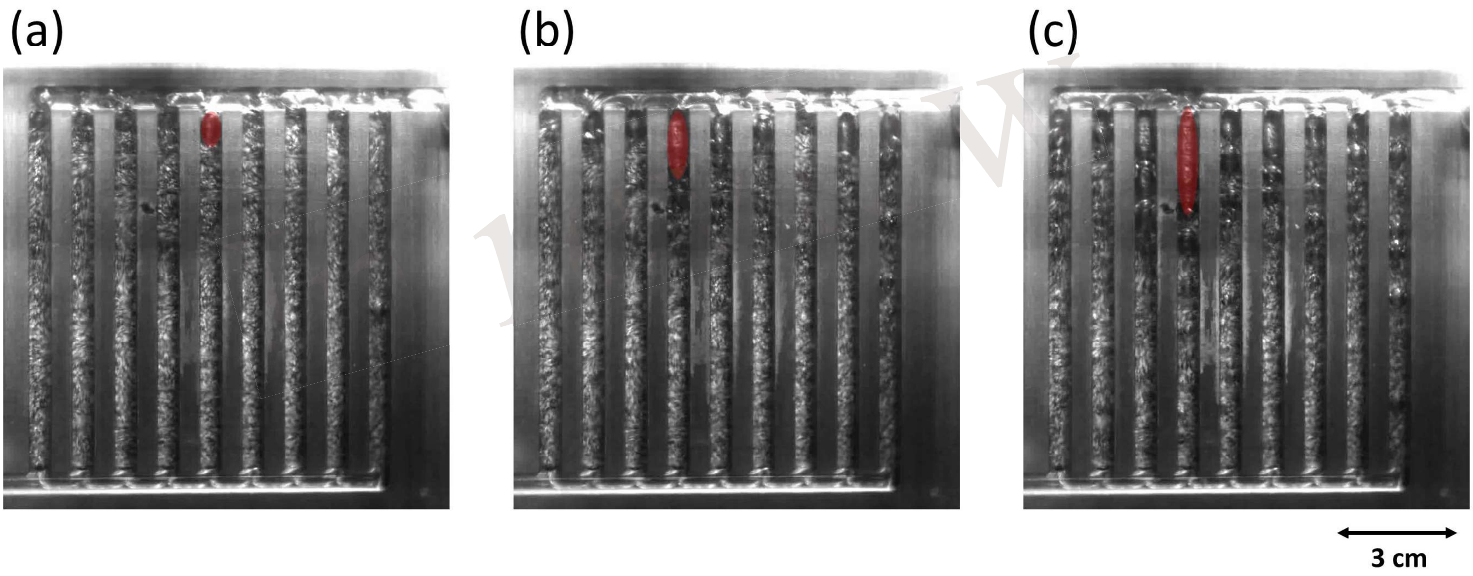

Figure 4.JPEG